Supercond. Sci. Technol. **XX** (XXXX) XXXXXX https://doi.org/XXXX/XXXX

In-depth S/TEM observation of Ti–Hf and Ta–Hf-doped Nb_3Sn layers

Nobuya Banno[1], Taku Moronaga[2], Toru Hara[3], Koki Asai[1,4] and Tsuyoshi Yagai[4]

[1] Research Center for Energy and Environmental Materials, National Institute for Materials Science (NIMS), Tsukuba, Japan
[2] Research Network and Facility Services Division, National Institute for Materials Science (NIMS), Tsukuba, Japan
[3] Research Center for Structural Materials, National Institute for Materials Science (NIMS), Tsukuba, Japan
[4] Faculty of Science and Technology, Sophia University, Tokyo, Japan

E-mail: banno.nobuya@nims.go.jp

Received xxxxxx
Accepted for publication xxxxxx
Published xxxxxx

Abstract

In superconducting Nb_3Sn layers with coherence lengths of approximately 3 nm, grain boundaries act as effective pinning sites. Thus, grain refinement is an essential issue that directly affects the superconducting critical characteristics of the Nb_3Sn layer. In recent years, Hf addition to Nb_3Sn wires co-doped with Ta has attracted notable interest as a method that enables grain refinement down to several tens of nm. In-depth characterization of the Nb_3Sn grain morphology in Hf-doping is crucially important to correlate the microstructure with the flux pinning characteristics. In this article, the grain morphologies of Ti–Hf and Ta–Hf-doped Nb_3Sn layers were clarified by scanning transmission electron microscopy (STEM) and TEM-based automated crystal orientation mapping (ACOM-TEM). STEM/energy dispersive X-ray spectroscopy (EDS) revealed no significant oxide precipitates in our samples. The grain size distribution was attained by ACOM-TEM. Although Hf-doping attained a grain refinement effect in the Nb_3Sn layer in both doping cases, the degree of this effect was relatively small for Ti–Hf. Kernel average misorientation (KAM) analysis by scanning electron microscopy-electron backscatter diffraction (SEM-EBSD) unveiled no appreciable difference between the internal strain states of the Nb-alloy parent phases in Ti–Hf and Ta–Hf. One remarkable new finding through STEM/EDS was the presence of a Cu–Hf compound phase in the Nb_3Sn layer. The Cu–Hf compound sounds analogous to the Cu–Ti compounds that form when Nb–47Ti with Cu matrix is heat treated. The STEM/EDS maps revealed a larger amount of Cu flow from the Cu-Sn side along the grain boundaries. The large Cu deposition on the grain boundaries might facilitate grain growth in Nb_3Sn. Those findings make a novel contribution to the literature as they provide a deep insight into Nb_3Sn phase formation via Hf doping.

Keywords: Nb_3Sn, Hf doping, ACOM-TEM, TEM, Grain growth

1. Introduction

Nb_3Sn superconducting wires are integral components of high-field magnet systems such as NMR spectroscopes [1], fusion magnets [2–5], and acceleration magnets [6,7]. At

 © xxxx IOP Publishing Ltd

present, a big scientific project to build a large high-energy particle collider 100 km in circumference, called the Future Circular Collider (FCC) [6,7], has attracted particular interest in the field of Nb_3Sn wire development. The project demands a performance of 1500 A/mm^2 at 16 T for the conductor at the industrial level, which is critically challenging because thermodynamical and cross-sectional geometric design optimization for Nb_3Sn layer formation seems to be almost accomplished.

As a breakthrough, two methods for refining the Nb_3Sn grain morphology during the Nb/Sn diffusion reaction have been proposed recently; the internal oxidation technique for the parent Nb phase [8–11], and Hf–Ta co-addition to Nb [12]. In the internal oxidation method, the formation of nano-scale oxide particles plays a pinning role during Nb_3Sn grain growth; these particles also act as flux pinning centers under current operation in magnetic fields [10]. Hf-addition effectively increases the nucleation frequency owing to the introduction of nanostructures, such as dislocations or local misorientations, within grains in the parent Nb phase [12,13], while Ta is co-doped to improve the critical magnetic field (B_{c2}) [9,12].

Ta and Ti have long been known as effective elements for augmenting the B_{c2} value [14–18]; however, a Ta content almost twice that of Ti is needed to obtain a similar improvement. A study of the doping mechanism has indicated that the site displacement behavior in the Nb_3Sn lattice differs between these elements. Extended X-ray absorption fine structure (EXAFS) measurements revealed that Ti atoms are preferentially localized in Nb sites, whereas Ta atoms can sit in both Nb and Sn sites [19,20]. This phenomenon may account for the difference in the enhancement of B_{c2} when doping with these elements. Using 3D atom probe tomography [21], Tarantini reported the presence of numerous nanocrystalline HfO_2 phases in the grains of the first Hf–Ta doped Nb_3Sn wire reported by Balachandran [12]. This specimen was fabricated by a powder-in-tube (PIT) technique, which might provide oxygen sources via the decomposition of the oxide layers on the powders. Thus, it is still argued that the grain refinement and additional flux pinning effect may have been caused by the same mechanism as that of internal oxidation. Meanwhile, it was confirmed that the microstructure of the parent Nb layer definitely affects the Nb_3Sn microstructure formation by simple experiments using as-drawn fine microstructural Nb–Ta–Hf alloys and fully-recovered Nb–Ta–Hf alloys [13]. Xu also examined the effect of Hf-addition on grain refinement for a sample fabricated by the PIT process under no oxidation source conditions [22]. On the contrary, Bovone has recently reported that there was no significant grain refinement by Hf-addition in a sample fabricated by the rod-in-tube method [23]. Thus, the effect of Hf-doping on the Nb_3Sn layer formation still appears to be ambiguous.

In this context, the first aim in this study is to prove the effect of Hf doping in no-oxygen conditions and increase the creditability of the past results [12,22,23]. The second objective is to clarify the difference in the Nb_3Sn layer development between Ti and Ta co-doping with Hf. For these purposes, in this study, specimens were fabricated by an electroplating technique to achieve easily and relatively homogenous Nb/Cu/Sn diffusion couples and prevent oxygen contamination as much as possible. In the observation of the grain morphology of the Nb_3Sn layer, scanning transmission electron microscopy (STEM) was applied with energy dispersive X-ray spectroscopy (EDS) to identify the formed phases. TEM-electron energy loss spectroscopy (EELS), which tends to work better at relatively low atomic numbers than EDS, was also performed as a complemental check of the composition. Furthermore, a TEM-based automated crystal orientation mapping (ACOM-TEM) method was used to attain the grain size distribution. Moreover, differences in the internal strain state of the parent Nb-alloy phase with respect to the doping elements was evaluated through scanning electron microscopy (SEM)/electron backscattered diffraction (EBSD) analysis.

In conclusion, no significant oxide nanoprecipitates were observed in our specimens. Then, it was confirmed that Hf-doping has a grain refinement effect in the Nb_3Sn layer in both cases of Ti–Hf and Ta–Hf doping; however, notably, some difference was observed in the degree of the effect. Ti–Hf doping demonstrated a relatively small impact. In addition, grain growth was observed even in the Ta–Hf doped specimen, depending on the position in the Nb_3Sn layer. The Cu diffusion might be accelerated in Hf doping when Cu content in the Cu–Sn side is increased, facilitating Nb_3Sn grain growth.

2. Method

2.1 Nb_3Sn specimen preparation

The precursor wires of the Nb_3Sn specimens were prepared by an electroplating technique. First, bars of Nb-alloys (Nb–2at%Ti–1at%Hf and Nb–4at%Ta–1at%Hf) that act as a parent phase in Nb_3Sn formation, were prepared by arc-melting. The Nb-alloy bars were re-arc-melted after plastic deformation to better homogenization. The Nb-alloy bars were then swaged into a cylindrical shape with a diameter of approximately 5.8 mm. The bars were inserted into a Cu tube with an outer/inner diameter of 8/6 mm, and cold-drawn by swaging and die-drawing into composite wires with a diameter of 1.09 mm. The true strain due to drawing is approximately 4.0. The wires were then flat-rolled into tapes with a thickness of approximately 0.18 mm.

Sn layers were electroplated on the tapes. The amount of Sn was controlled, measuring the weight so that the atomic ratio of the Cu sheath and Sn layer is 0.75:0.25. The Cu cross-sectional areas were measured on the transverse cross-

sectional images taken by a SEM (SU-70, Hitachi), using image analysis software (ImageJ, Wayne Rasband). The Sn atomic composition was chosen to be 25% because of preventing Nb_6Sn_5 development in case of the Sn composition over 25% in the diffusion reaction stage between Cu–Sn and Nb-alloy [24,25]. Reportedly, Nb_6Sn_5 decomposes into coarse Nb_3Sn grains with less intergranular connections [26,27], which would be a source of uncertainty in the analysis.

The Sn-electroplated specimens were subsequently encased in a silica capsule filled with Ar gas. The specimens were pre-annealed at 550 ºC for 100 h and then heat-treated at 685 ºC for 100 h for Nb_3Sn formation. The former stage of the heat treatment is devoted to mix the Cu and Sn [25]. Nb_3Sn was then developed through diffusion reaction between the Cu–Sn and Nb-alloy: Nb_3Sn layer is primarily formed on the Nb-alloy parent phase because of the faster diffusion rate of Sn. The average Nb_3Sn layer thickness was also measured by

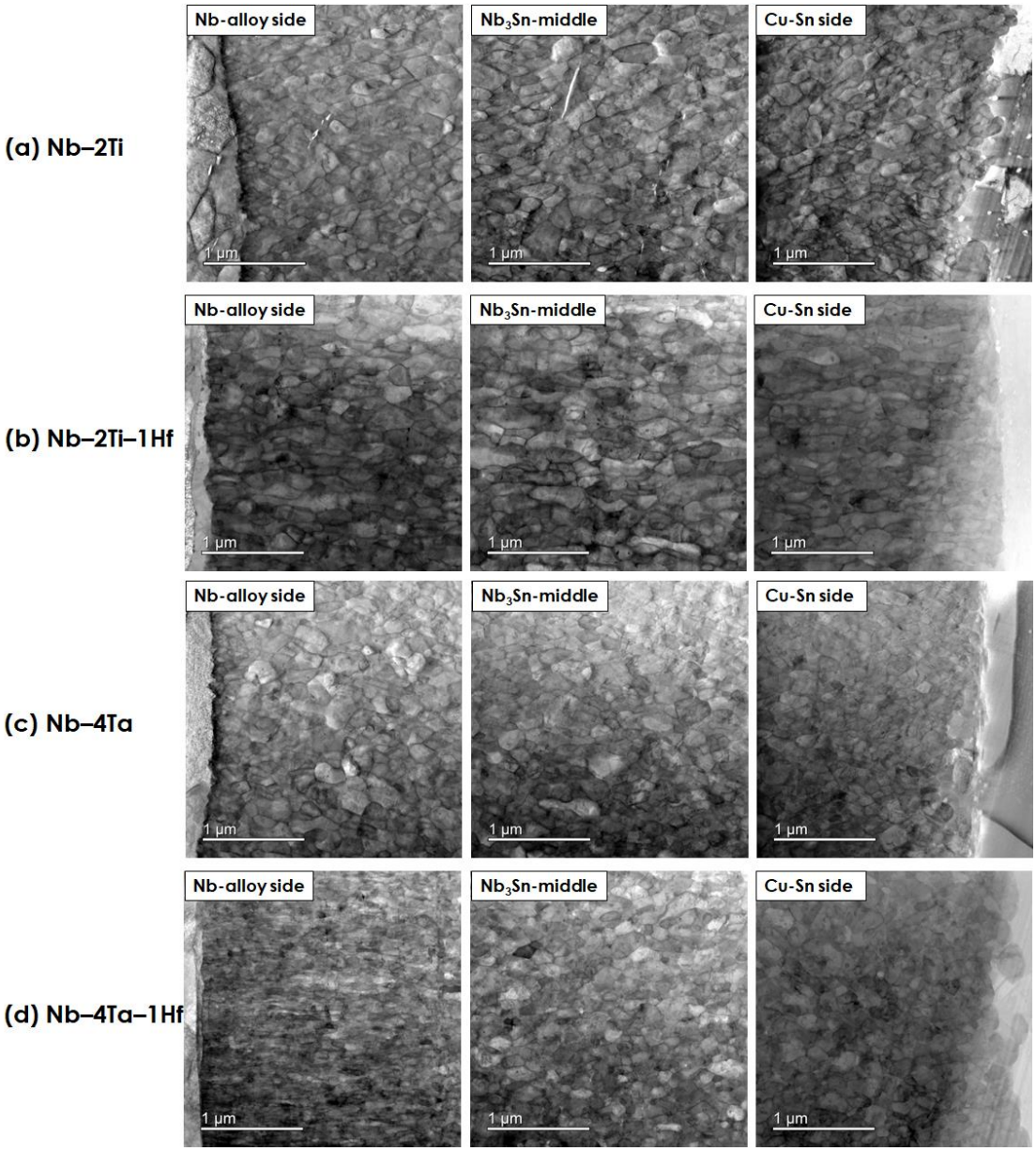

Figure 1. STEM BF images (acc: 200 kV) of formed Nb_3Sn layers in (a) 2Ti doped, (b) 2Ti–1Hf co-doped, (c) 4Ta doped, and (d) 4Ta–1Hf co-doped. The left images represent the grain morphologies near the reaction front, the center ones around the middle of the layer, and the right ones near the Cu–Sn side.

an image analysis (ImageJ), using SEM images of the transverse cross-section: more than a hundred thicknesses were measured and averaged per sample.

2.2 S/TEM observation

Ultra-thin samples with 10–20 μm in width and 5–10 μm in height were cut out by focused ion beam from fine polished transverse cross-sections of the heat-treated Nb_3Sn specimens. To see the overall microstructures of the Nb_3Sn layer, the samples include thin areas of Nb-alloy and Cu-Sn compound layers at both sides perpendicular to the diffusion direction.

The microstructures were observed by two S/TEMs (JEM-2800 with an accelerator voltage (acc) of 200 kV, and JEM-ARM300F with acc of 300 kV, JEOL) that have been installed at Research Network and Facility Services Division in NIMS. The JEM-2800 is equipped with ACOM-TEM system, while the JEM-ARM300F is equipped with EDS system.

2.3 Grain size analysis by ACOM-TEM

Grain size was analyzed by the ACOM-TEM method (ASTAR™ system, NanoMEGAS), which is a method for obtaining crystal orientation maps and phase maps similar to the SEM/EBSD method in a TEM. ASTAR™ combines precession electron diffraction to collect stable diffraction patterns, which allows orientation or phase mapping with a resolution down to 1 nm (specimen dependent). Diffraction patterns are indexed using NanoMEGAS's patented template matching method to calculate crystal orientation and determine phase (crystal system).

In collecting the grain maps, first, the areas with low analysis accuracy due to reasons such as pattern overlap (OR (orientation reliability) <2) were removed from the raw data. The measurement step was 2.5 nm. Therefore, the grains no more than 5 nm (consisting of only one or two measurement points) were taken off as anti-grain because of unreliability. Finally, the dropout areas with 1 pixel were filled, using the surrounding data.

2.4 EBSD analysis

The transverse cross-section of samples was first polished with polycrystalline diamond suspensions and then chemo-mechanically polished with non-crystallizing amorphous 0.05 and 0.02 μm colloidal silica suspensions (MasterMet, Buehler) in the final steps. The cross-sections were then thoroughly cleaned with a neutral cleanser. Raw EBSD data were refined using the neighbor CI correlation method with a threshold of CI=0.1. The minimum misorientation angle used to determine the grain boundaries was set to 5°.

In order to determine the internal strain state, grain orientation spread (GOS) or kernel average misorientation (KAM) is often analyzed [5,25,28,29]. Here, KAM was analyzed. KAM is the index expressing the local average grain orientation difference at a given pixel defined as

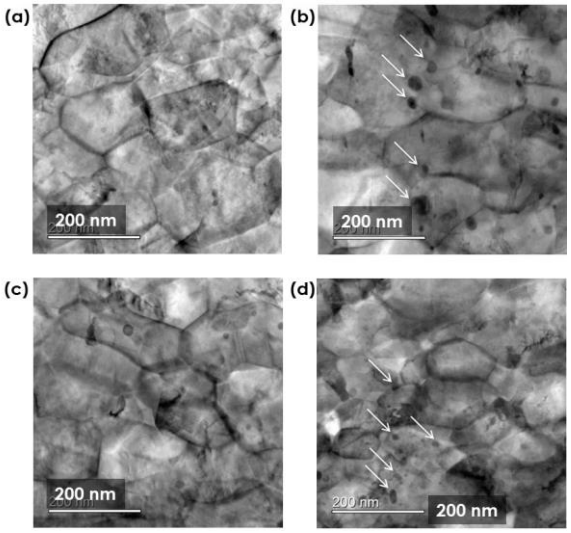

Figure 2. Characteristic magnified STEM BF images (acc: 200 kV) of formed Nb_3Sn layers in (a) 2Ti doped, (b) 2Ti–1Hf co-doped, (c) 4Ta doped, and (d) 4Ta–1Hf co-doped. In Hf doped specimens, some kind of nanoprecipitate is identified. A few small spots seen in the 4Ta-doped specimen were confirmed by detailed analysis to be not precipitates, but rather areas where a portion of another grain is superimposed in thickness.

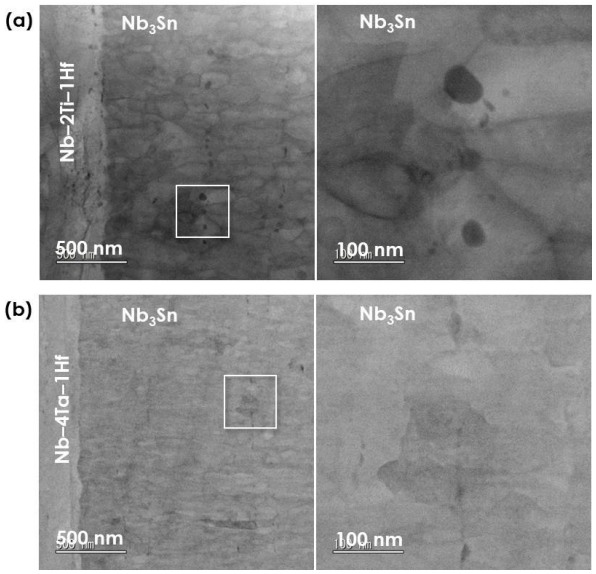

Figure 3. STEM BF images (acc: 300 kV) of Nb_3Sn layers near the reaction front in (a) 2Ti–1Hf and (b) 4Ta–1Hf co-doped.

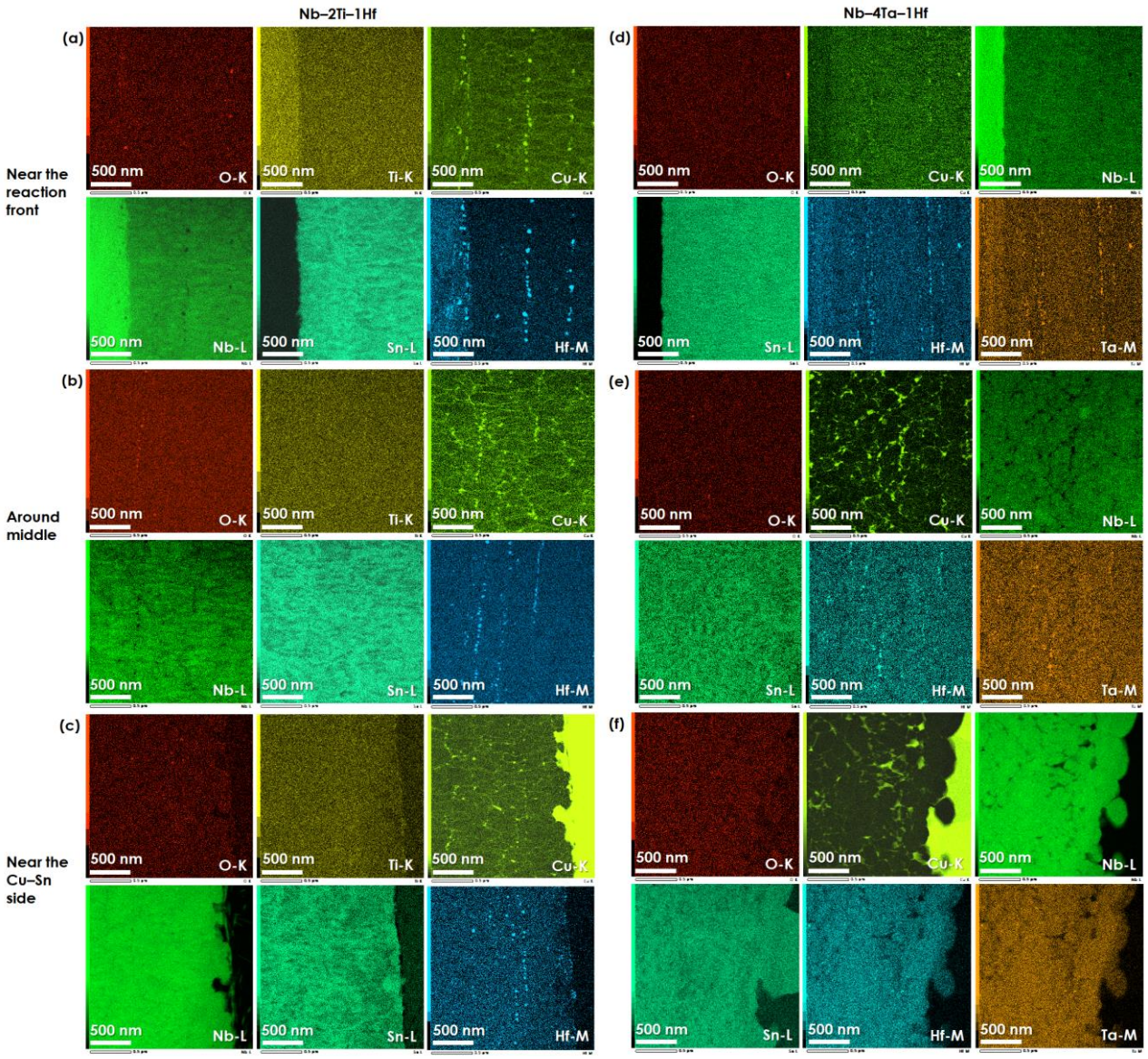

Figure 4. STEM-EDS elemental maps of the Nb_3Sn layers. (a), (b) and (c) indicate the maps near the reaction front, around middle and near the Cu–Sn side in Ti–Hf, and (d), (e) and (f) the maps near the reaction front, around middle and near the Cu–Sn side in Ta–Hf doped samples.

$$\mathrm{KAM} = \sum_{i=1}^{6} \alpha_i / 6, \qquad (1)$$

where α_i is the orientation difference between a given pixel and the *i*-th neighboring pixel. The local crystal orientation change within a grain is thought to be caused by the internal strain. Therefore, KAM is likely to reflect the internal strain energy.

3. Results

3.1 Grain morphology and element maps

Figure 1 exhibits STEM bright field (BF) images of the formed Nb_3Sn layers in (a) 2Ti, (b) 2Ti–1Hf, (c) 4Ta, and (d) 4Ta–1Hf doping. The left, center, and right images indicate the maps near the reaction front, around the middle, and near the Cu–Sn side, respectively. STEM images taken at the acceleration voltage of 200 kV are usually expressed in

Table 1. Analyzed results of Nb_3Sn grain size by ACOM-TEM

Sample	1	2	3	4
Additive	2Ti	2Ti–1Hf	4Ta	4Ta–1Hf
Grain size (nm)				
Reaction front	171.6	145.1	111.0	69.7
Middle	150.6	150.3	101.3	121.8
Cu–Sn side	167.7	134.1	98.7	158.2

greater contrast than at 300 kV due to interference with the sample. A quick view of the microstructure shows that the Ta–Hf-doped sample appears to have a fine microstructure. A detailed analysis of grain size is presented in Section 3.2.

Figure 2 demonstrates characteristic magnified STEM BF images (acc: 200 kV) in (a) 2Ti, (b) 2Ti–1Hf, (c) 4Ta, and (d) 4Ta–1Hf doped specimens. In the Hf doped specimens, some kind of nanoprecipitates were identified. Figure 3 exhibits additional examples of BF images (acc: 300 kV) of the Nb_3Sn layer near the reaction front in Ti–Hf and Ta–Hf co-doping, which more clearly unveil the presence of precipitates. The precipitates dwell primarily at grain boundary triple points. The size of the precipitates appears to be larger in Ti–Hf doping.

Figure 4 shows STEM-EDS elemental maps of the Nb_3Sn layers in Ti–Hf and Ta–Hf doped samples. Notably, the elemental maps indicate no significant oxide precipitate, while suggesting the presence of Cu–Hf nano-compound. In Ta–Hf

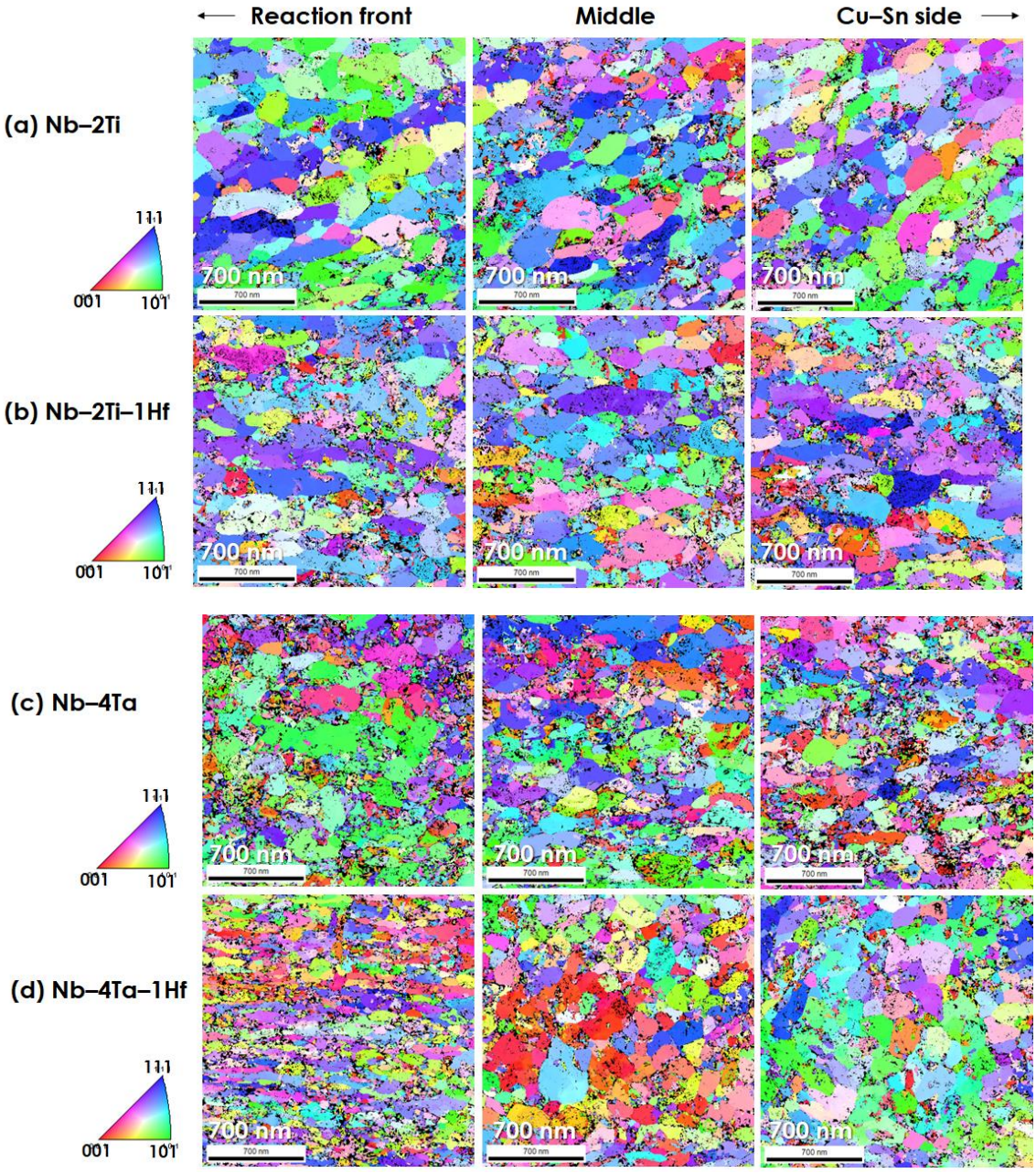

Figure 5. Inverse pole figure (IPF) maps of Nb_3Sn layer in (a) 2Ti, (b) 2Ti–1Hf, (c) 4Ta, and (d) 4Ta–1Hf doped, taken by ACOM-TEM. The left, center and right images indicate the maps near the reaction front, around the middle, and near the Cu–Sn side, respectively.

doping, the Cu–Hf compound seems to include Ta as shown in Figure 4 (d). At the middle and near the Cu–Sn side, the deposition of Cu on the grain boundaries appears to be more pronounced, accompanied by a small amount of Hf and Ta (Figure 4 (b), (c), and (e)); in the Ta–Hf doping sample, while a large amount of Cu segregates along grain boundaries near the Cu–Sn side, Hf and Ta seems to be taken away (Figure 4 (f)).

3.2 Grain size distribution

Figure 5 plots inverse pole figure (IPF) maps of Nb_3Sn layer in (a) 2Ti, (b) 2Ti–1Hf, (c) 4Ta, and (d) 4Ta–1Hf doping, taken by the ACOM-TEM method. The left, center and right images indicate the maps near the reaction front, around the middle, and near the Cu–Sn side, respectively. Analyzed results of the grain size are summarized in Table 1.

As far as paying attention to the reaction front, the grain size tends to be refined by Hf addition in both Ti and Ta doped samples. As above-mentioned, since no significant oxide nanoprecipitation is present, this grain refinement is believed to reflect the pure impact of the Hf-addition. The reason for determination of the relatively small grain size in the sample 3 is thought to be due to a large number of noise-like small low-quality areas. Careful view of Figure 5 (c) reveals that while many coarse grains are observable, there are also substantial small areas. Presumably, the grain size of sample 3 is actually larger. Nevertheless, across the whole area, the grain size of the Ta doped samples tends to be smaller than that of the Ti doped samples. Noteworthy, comparing Ti doping with Ta doping, the impact of Hf co-doping on grain refinement is likely to be larger for Ta doping in the reaction front. The grain size in Ta–Hf doped specimen however appears to be increasing near the Cu–Sn side as shown in the right map of Figure 5 (d) and Table 1.

3.4 Nb_3Sn layer thickness

Figure 6 depicts SEM images of typical Nb_3Sn layer for each sample. The Nb_3Sn layer thicknesses are measured as 8.07, 11.87, 8.2, and 15.4 μm for Ti, Ti–Hf, Ta, and Ta–Hf doped samples, respectively. The Nb_3Sn layer is essentially formed through grain boundary diffusion of Sn [30,31]. Reflecting this, there can be seen a tendency for the layer thickness to increase with decreasing grain size. In reality, the phenomenon is probably more complicated due to grain boundary precipitation and other effects.

4. Discussion

According to a classic nucleation theory, the Gibbs energy change ΔG, when a spherical phase is nucleated on a parent phase, can be described as [32]:

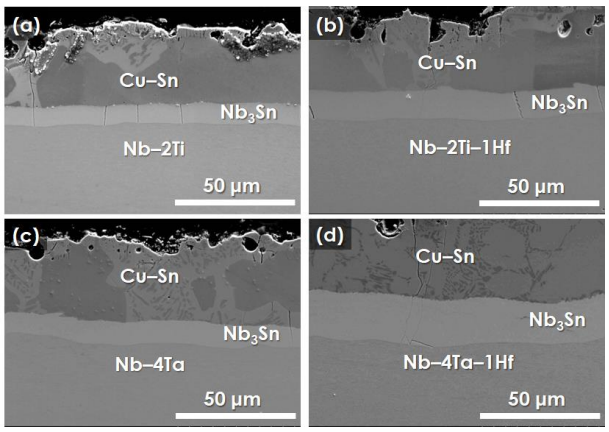

Figure 6. SEM backscattered electron images (acc: 20 kV) of Nb_3Sn layers in (a) Ti, (b) 2Ti–1Hf, (c) Ta and (d) 4Ta–1Hf doped.

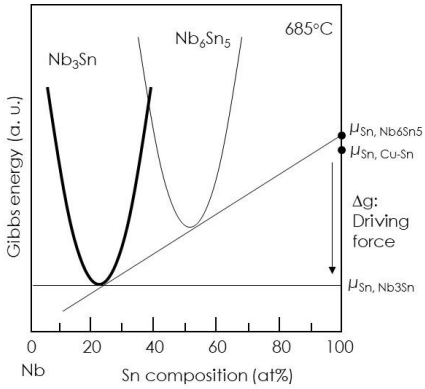

Figure 7. Schematic illustration of relationship between Gibbs energy and Sn chemical potential, μ, at a given Nb_3Sn formation temperature. $\mu_{Sn,\ Nb6Sn5}$ denotes the Sn chemical potential when the Nb_6Sn_5 and Nb_3Sn coexist at an equilibrium condition. $\mu_{Sn,\ Cu–Sn}$ indicates the Sn chemical potential in Cu–Sn, when the Sn composition is slightly less than 25 at%. $\mu_{Sn,\ Nb3Sn}$ denotes the Sn chemical potential in the stable Nb_3Sn.

$$\Delta G = \left(\frac{-4\pi r^3}{3}\right)\left(\frac{\Delta g}{v}\right) + 4\pi r^2\sigma, \qquad (2)$$

where Δg, r, v, and σ represent the chemical potential difference, radius of the precipitate particle, volume of the precipitate particle per mole, and surface energy density, respectively. ΔG peaks at a radius, that is the critical nuclear radius ($r_c = 2\sigma v/\Delta g$ obtained under the condition $\partial\Delta G/\partial r = 0$) of the precipitate particle. Thus, grain size is essentially reduced with an increase of Δg: Δg is regarded as the driving force for the nucleation. The relationship between the Sn chemical potential and the Gibbs energy of Nb_3Sn in Nb–Sn system at a given Nb_3Sn formation temperature of 685 °C can

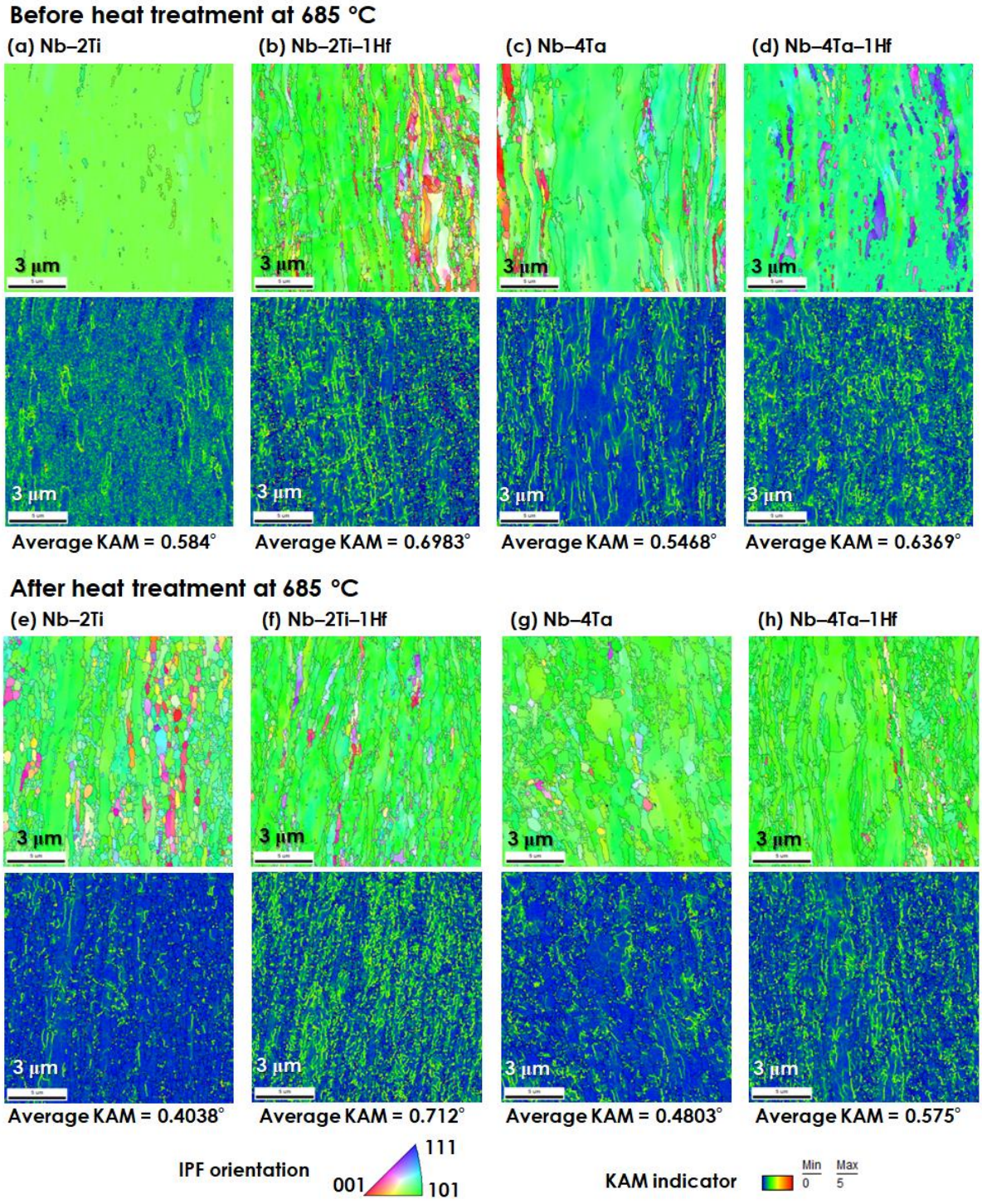

Figure 8. IPF with grain boundary (upper) and KAM (lower) maps of parent Nb-alloy before and after heat-treatment at 685 °C for 100 h: (a) 2Ti, (b) 2Ti–1Hf, (c) 4Ta, and (d) 4Ta–1Hf doping before heat-treatment, and (e) 2Ti, (f) 2Ti–1Hf, (g) 4Ta, and (h) 4Ta–1Hf doped after heat-treatment.

be schematically illustrated like Figure 7. Reportedly, Hf addition raises the recrystallization temperature of the parent Nb-alloy phase, by which the parent Nb-alloy phase maintains the fine grain microstructure such as dislocation induced by cold-working at Nb_3Sn formation temperatures around 650 °C [12,13]. The cold-working-induced fine microstructure is

believed to have a high internal strain energy, which should increase the Nb_3Sn nucleation driving force. Qualitatively, it can be explained that the additional internal strain energy by Hf addition causes grain refinement of Nb_3Sn.

The internal strain state can be represented by measuring KAM values in EBSD. To reveal the internal strain state of the parent Nb-alloy phase, IPF and KAM maps were created before and after heat treatment, as shown in Figure 8. The average KAM values over the measured area in all specimens were high before heat treatment at 685 °C for 100 h. Especially, the specimens with Hf co-doping exhibited higher KAM values, compared with no Hf doping. Furthermore, while the specimens with no Hf doping demonstrated a decrease in the average KAM values, the Hf co-doped specimens sustained high KAM values even after the heat treatment. This confirms the effect of Nb_3Sn grain refinement by Hf addition.

As described in section 3.1, nano-scale Cu–Hf compound particles were present in the Nb_3Sn region near the reaction front, especially at grain boundary triple points for Ti–Hf and Ta–Hf doped specimens. However, the frequency of Cu–Hf precipitates does not appear to be high enough to cause the Zener pinning effect, compared with the oxide particle distribution in Nb_3Sn developed by the internal oxidation technique [10].

As one reason for the relatively small effect of Ti–Hf addition on grain refinement compared with Ta–Hf addition, a decrease of the internal strain energy was considered in Ti–Hf doped specimen. However, there was no significant difference in the average KAM value between them, rather Ti–Hf doped specimen demonstrated a higher KAM value even after heat treatment. Therefore, the internal strain energy does not explain the reason for the smaller impact on the grain refinement in Ti–Hf.

Another possibility for this was a variation in the Gibbs energy of Nb_3Sn due to the solid solution of Ti into Nb_3Sn. Reportedly, the behavior of site substitution into the Nb_3Sn lattice is different for Ti and Ta [19,20]: Ti atoms are always allocated at Nb sites, while Ta atoms can locate the Sn sites as well as Nb sites. Such a difference in the substitution behavior might affect the Gibbs energy of Nb_3Sn. However, some reports suggest that the presence of Ti does not lead to a significant change in Nb_3Sn grain size, compared to no Ti doping [32,33]. It indicates that the substitution by Ti or Ta is unlikely to bring about a substantial impact on the Nb_3Sn Gibbs energy and thus the nucleation driving force.

The final discussion for the smaller impact on the Nb_3Sn grain refinement in Ti–Hf concerns the influence on grain growth. As shown in Figure 3, the Cu–Hf precipitates near the reaction front are appreciably larger in Ti–Hf doped specimen than those in Ta–Hf doped. Furthermore, a closer look at Figure 4 (a) noticeably reveals high contrast of Cu along grain boundaries in Ti–Hf doping over the entire Nb_3Sn region.

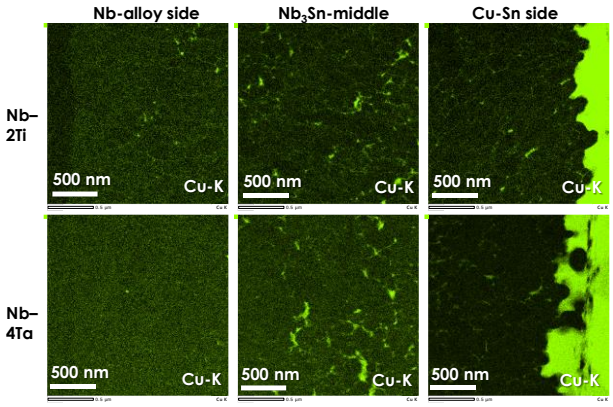

Figure 9. STEM-EDS elemental maps (Cu) of the Nb_3Sn layers in 2Ti- and 4Ta-doped specimens near the reaction front, around middle and near the Cu–Sn side.

These findings suggest that Ti–Hf doping tends to facilitate Cu diffusion along grain boundaries, compared with Ta–Hf doping. In general, grain growth is a phenomenon accompanied by a decrease in the surface energy of grains. The large Cu deposition on grain boundaries might contribute to destabilizing the grain surface and thus grain coarsening. This is thought to have slightly counteracted the grain refinement effect by the Hf addition in Ti–Hf doping. That appears to be the most possible reason for the smaller effect on the grain refinement in Ti–Hf.

The additional discussion is regarding the grain growth of Nb_3Sn in the Ta–Hf doped specimen in the middle and near the Cu–Sn side. A closer look at Figure 4 (e) and (f) reveals a high Cu concentration along grain boundaries as well as in the Ta–Hf doped specimen. Reportedly, Cu content at the grain boundary is approximately 10 at%, and the thickness is approximately 2 nm in conventional Nb_3Sn wires [34,35]. Figure 9 shows Cu elemental maps of the Nb_3Sn layers in 2Ti- and 4Ta-doped specimens near the reaction front, around middle and near the Cu–Sn side, taken by STEM-EDS. Comparing the Cu elemental maps between 4Ta doping and 4Ta–1Hf doping, the Cu segregation at Nb_3Sn grain boundaries in Ta–Hf doped specimens are found to be more significant, especially near the Cu–Sn side. This finding supports the fact that increased Cu diffusion coarsens the grains, resulting in a grain size near the Cu–Sn side in the Ta–Hf doped sample that exceeds that of the no Hf doped. Why Cu diffusion near the Cu–Sn side in the Ta–Hf doped sample is more pronounced than that in the Ti–Hf doped sample is still an open question. The effect of heat treatment temperature should also be considered in the next step.

Hf might have an effect of promoting Cu grain boundary diffusion, regardless of whether it is Ti-co-doped or Ta-co-doped. Recently, we also reported that the grain refinement effect was considerably small in bronze-route Hf doped Nb_3Sn

[36,37]. As a possibility, it could be suggested that the Cu diffusion is accelerated in Hf doping when Cu content in Cu–Sn side is increased like bronze-route Nb_3Sn, advancing Nb_3Sn grain growth.

5. Conclusion

The STEM, EDS, and ACOM-TEM analysis of Ti–Hf and Ta–Hf-doped Nb_3Sn layers demonstrated the following findings. First, the grain morphologies of the Hf-doped Nb_3Sn that were developed by diffusion reaction between Nb-alloy and Cu–25at%Sn, were found to be finer near the reaction front, compared with no Hf doping. In the specimens tested in this study that were prepared by an electroplating method, no significant oxide nanoprecipitate was detected. Thus, Hf-addition was proven to contribute to the grain refinement of Nb_3Sn without oxide nanoprecipitates. The primary reason for the grain refinement is thought to be due to the increase in internal strain energy of the Nb-alloy parent phase induced by cold-working, which contributes to promoting the Nb_3Sn phase nucleation.

However, the impact on the grain refinement by Hf-addition was relatively smaller in Ti–Hf doping than in Ta–Hf doping. In the Hf-doped specimens, Cu–Hf compound particles were detected primarily on grain boundary triple points near the reaction front. Furthermore, high contrast of Cu was found even along grain boundaries in Ti–Hf doping. The large Cu deposition on grain boundaries might contribute to destabilizing the grain surface and thus grain coarsening. This is thought to have slightly counteracted the Nb_3Sn grain refinement effect by the Hf addition in Ti–Hf doping.

It is worth noting that, in Ta–Hf doped specimen, Nb_3Sn grain growth was recognized in the middle and near the Cu–Sn side. High Cu concentration was detected along grain boundaries in the middle and near the Cu–Sn in the Ta–Hf doped sample as well as in the Ti–Hf doped sample. Hf might have an effect of promoting Cu grain boundary diffusion, regardless of whether it is Ti-co-doped or Ta-co-doped. The Cu diffusion seems to be accelerated in Hf doping when the Cu content in the Cu–Sn side is increased, advancing Nb_3Sn grain growth.

Acknowledgements

This work was partially supported by JSPS KAKENHI Grant Number JP23K04453.

References

[1] Miyazaki T, Miyatake T, Kato H, Zaitsu K, Murakami Y, Hase T and Hamada M 2008 Development of Nb_3Sn superconducting wires for high field magnets at Kobe Steel and JASTEC *Cryogenics (Guildf)* **48** 341–6

[2] Devred A, Backbier I, Bessette D, Bevillard G, Gardner M, Jong C, Lillaz F, Mitchell N, Romano G and Vostner A 2014 Challenges and status of ITER conductor production *Supercond Sci Technol* **27** 044001

[3] Mitchell N, Breschi M and Tronza V 2020 The use of Nb_3Sn in fusion: lessons learned from the ITER production including options for management of performance degradation *Supercond Sci Technol* **33** 054007

[4] Bruzzone P, Sedlak K, Sarasola X, Stepanov B, Uglietti D, Wesche R, Muzzi L and Della Corte A 2018 A prototype conductor by react&wind method for the EUROfusion DEMO TF coils *IEEE Transactions on Applied Superconductivity* **28** 4202705

[5] Banno N, Yagai T, Kawashima S, Sugimoto M, Awaji S, Utoh H and Skamoto Y 2023 Metallographic and bending strain property analysis for DEMO candidate Nb_3Sn wires in Japan *IEEE Transactions on Appiled Superconductivity* submitted

[6] Ballarino A and Bottura L 2015 Targets for R&D on Nb_3Sn conductor for high energy physics *IEEE Transactions on Applied Superconductivity* **25** 6000906

[7] Schoerling D, Arbelaez D, Auchmann B, Bajko M, Ballarino A, Barzi E, Bellomo G, Benedikt M, Bermudez S I, Bordini B, Bottura L, Brouwer L, Bruzzone P, Caiffi B, Caspi S, Chakraborti A, Coatanea E, De Rijk G, Dhalle M, Durante M, Fabbricatore P, Farinon S, Felice H, Fernandez A, Fernandez I S, Gao P, Gold B, Gortsas T, Gourlay S, Juchno M, Kashikhin V, Kokkinos C, Kokkinos S, Koskinen K, Lackner F, Lorin C, Loukas K, Louzguiti A, Lyytikainen K, Mariotto S, Marchevsky M, Montenero G, Munilla J, Novitski I, Ogitsu T, Pampaloni A, Perez J C, Pes C, Petrone C, Polyzos D, Prestemon S, Prioli M, Ricci A M, Rifflet J M, Rochepault E, Russenschuck S, Salmi T, Santillana I A, Savary F, Scheuerlein C, Segreti M, Senatore C, Sorbi M, Statera M, Stenvall A, Tavian L, Tervoort T, Tommasini D, Toral F, Valente R, Velev G, Verweij A P, Wessel S, Wolf F, Zimmermann F and Zlobin A V. 2019 The 16 T Dipole Development Program for FCC and HE-LHC *IEEE Transactions on Applied Superconductivity* **29**

[8] Xu X, Sumption M, Peng X and Collings E W 2014 Refinement of Nb_3Sn grain size by the generation of ZrO_2 precipitates in Nb_3Sn wires *Appl Phys Lett* **104** 082602

[9] Xu X, Rochester J, Peng X, Sumption M and Tomsic M 2019 Ternary Nb_3Sn superconductors with artificial pinning centers and high upper critical fields *Supercond Sci Technol* **32** 02LT01

[10] Xu X, Peng X, Rochester J, Lee J Y and Sumption M 2020 High critical current density in internally-oxidized Nb_3Sn superconductors and its origin *Scr Mater* **186** 317–20

[11] Rochester J, Ortino M, Xu X, Peng X and Sumption M 2021 The Roles of Grain Boundary Refinement and Nano-Precipitates in Flux Pinning of APC Nb_3Sn *IEEE Transactions on Applied Superconductivity* **31** 8000205

[12] Balachandran S, Tarantini C, Lee P J, Kametani F, Su Y F, Walker B, Starch W L and Larbalestier D C 2019 Beneficial influence of Hf and Zr additions to Nb4at%Ta on the vortex pinning of Nb_3Sn with and without an O source *Supercond Sci Technol* **32** 044006

[13] Banno N, Morita T, Yagai T and Nimori S 2021 Influence of parent Nb-alloy grain morphology on the layer formation of

Nb_3Sn and its flux pinning characteristics *Scr Mater* **199** 113822

[14] Tachikawa K, Asano T and Takeuchi T 1981 High-field superconducting properties of the composite-processed Nb_3Sn with Nb-Ti alloy cores *Appl Phys Lett* **39** 766–8

[15] Tachikawa K, Sekine H and Iijima Y 1982 Composite-processed Nb_3Sn with titanium addition to the matrix *J Appl Phys* **53** 5354–6

[16] Suenaga M, Tsuchiya K and Higuchi N 1984 Superconducting critical current density of bronze processed pure and alloyed Nb_3Sn at very high magnetic fields (up to 24 T) *Appl Phys Lett* **44** 919–21

[17] Suenaga M 1985 Optimization of Nb_3Sn *IEEE Trans Magn* **21** 1122–8

[18] Suenaga M, Welch D O, Sabatini R L, Kammerer O F and Okuda S 1986 Superconducting critical temperatures, critical magnetic fields, lattice parameters, and chemical compositions of "bulk" pure and alloyed Nb_3Sn produced by the bronze process *J Appl Phys* **59** 840–53

[19] Heald S M, Tarantini C, Lee P J, Brown M D, Sung Z, Ghosh A K and Larbalestier D C 2018 Evidence from EXAFS for Different Ta/Ti Site Occupancy in High Critical Current Density Nb_3Sn Superconductor Wires *Sci Rep* **8** 4798

[20] Tarantini C, Balachandran S, Heald S M, Lee P J, Paudel N, Choi E S, Starch W L and Larbalestier D C 2019 Ta, Ti and Hf effects on Nb_3Sn high-field performance: Temperature-dependent dopant occupancy and failure of Kramer extrapolation *Supercond Sci Technol* **32** 124003

[21] Tarantini C, Kametani F, Balachandran S, Heald S M, Wheatley L, Grovenor C R M, Moody M P, Su Y-F, Lee P J and Larbalestier D C 2021 Origin of the enhanced Nb_3Sn performance by combined Hf and Ta doping *Sci Rep* **11** 17845

[22] Xu X, Peng X, Rochester J, Sumption M D, Lee J, Calderon Ortiz G A and Hwang J 2021 The strong influence of Ti, Zr, Hf solutes and their oxidation on microstructure and performance of Nb_3Sn superconductors *J Alloys Compd* **857** 158270

[23] Bovone G, Buta F, Lonardo F, Bagni T, Bonura M, LeBoeuf D, Hopkins S C, Boutboul T, Ballarino A and Senatore C 2023 Effects of the oxygen source configuration on the superconducting properties of internally-oxidized internal-Sn Nb_3Sn wires *Supercond Sci Technol*

[24] Lachmann J, Kriegel M J, Leineweber A, Shang S-L and Liu Z-K 2022 Thermodynamic re-modelling of the Cu–Nb–Sn system: Integrating the nausite phase *Calphad* **77** 102409

[25] Banno N 2023 Low-temperature superconductors: Nb_3Sn, Nb_3Al, and NbTi *Superconductivity* **6** 100047

[26] Tarantini C, Segal C, Sung Z H, Lee P J, Oberli L, Ballarino A, Bottura L and Larbalestier D C 2015 Composition and connectivity variability of the A15 phase in PIT Nb_3Sn wires *Supercond Sci Technol* **28** 095001

[27] Segal C, Tarantini C, Sung Z H, Lee P J, Sailer B, Thoener M, Schlenga K, Ballarino A, Bottura L, Bordini B, Scheuerlein C and Larbalestier D C 2016 Evaluation of critical current density and residual resistance ratio limits in powder in tube Nb_3Sn conductors *Supercond Sci Technol* **29** 085003

[28] Morita T, Yagai T and Banno N 2022 Impact of Ti-doping position on Nb_3Sn layer formation in internal Sn-processed Nb_3Sn superconducting wires *Cryogenics (Guildf)* **122** 103420

[29] Santra S, Makineni S K, Shankar G, Suwas S, Chattopadhyay K, Divinski S V. and Paul A 2019 Insight into the effect of Ti-addition on diffusion-controlled growth and texture of Nb_3Sn intermetallic superconductor phase *Materialia (Oxf)* **6** 100276

[30] Togano K, Asano T and Tachikawa K 1979 Effects of magnesium addition to the CuSn matrix in the composite-processed Nb_3Sn superconductor *Journal of The Less-Common Metals* **68** 15–22

[31] Farrell H H, Gilmer G H and Suenaga M 1974 Grain boundary diffusion and growth of intermetallic layers: Nb_3Sn *J Appl Phys* **45** 4025–35

[32] Morita T, Banno N, Yagai T and Tachikawa K 2019 Microstructure and superconducting properties of brass matrix internal tin Nb3Sn wire with Ti doping to Nb core *IEEE Transactions on Applied Superconductivity* **29** 6001805

[33] Popova E N, Deryagina I L and Valova-Zaharevskaya E G 2014 The Nb_3Sn layers formation at diffusion annealing of Ti-doped multifilamentary Nb/Cu-Sn composites *Cryogenics (Guildf)* **63** 63–8

[34] Sandim M J R, Tytko D, Kostka A, Choi P, Awaji S, Watanabe K and Raabe D 2013 Grain boundary segregation in a bronze-route Nb_3Sn superconducting wire studied by atom probe tomography *Supercond Sci Technol* **26** 055008

[35] Banno N, Morita T, Yu Z, Yagai T and Tachikawa K 2019 Effect of Zn addition and Ti doping position on the diffusion reaction of internal tin Nb_3Sn conductors *Supercond Sci Technol* **32** 115017

[36] Morita T, Yagai T, Nimori S and Banno N 2022 Influence of Ti-Hf Doping on the Nb_3Sn Layer Formation in Bronze-Processed Nb3Sn Wire Structure *IEEE Transactions on Applied Superconductivity* **32**

[37] Banno N, Morita T, Yagai T and Nimori S 2022 Microstructure and superconducting properties of Hf–Ta addition bronze-route Nb_3Sn wire *IEEE Transactions on Applied Superconductivity* **32** 1–5